AIAA JOURNAL
Vol. 47, No. 4, April 2009

Aero-Micro-Electromechanical System Sensor Arrays for Time Resolved Wall Pressure Measurements

A. Berns,* U. Buder,† and E. Obermeier‡
Berlin Institute of Technology, 13355 Berlin, Germany
A. Wolter§ and A. Leder¶
University of Rostock, 18059 Rostock, Germany
and
O. Frederich** and F. Thiele††
Berlin Institute of Technology, 10623 Berlin, Germany

DOI: 10.2514/1.37256

Wall pressure and wall pressure fluctuations in turbulent flows are of interest in many engineering applications. This paper focuses on the design and fabrication of aero-micro-electromechanical system surface pressure sensor arrays and their application to wall pressure measurements on a wall-mounted cylinder. The sensor arrays have been developed to be highly sensitive and mounted flush with the measurement surface. Thus, dynamic properties of the sensors are not limited by tubing, and an accurate measurement of the wall pressure and its fluctuations becomes possible. The arrays introduced herein consist of a number of individual sensors, which feature a maximum sensitivity of 12 μV/(VPa) and a pressure resolution of up to 0.5 Pa. Employing six arrays (three different types) consisting of up to 13 individual pressure sensors, wall pressure measurements have been conducted at the University of Rostock at a Reynolds number of 200,000. The results prove that the developed sensor arrays are a powerful measurement tool for experimental fluid mechanics. The wall pressure measurement data obtained are in good agreement with the results of the laser Doppler anemometry measurements and large-eddy simulations, which are also presented herein.

Nomenclature

a	=	size of a square diaphragm
D	=	cylinder diameter
D_{dia}	=	diameter of a circular diaphragm
d	=	plate thickness
i	=	number of a finite element node inside V_{piezo}
L	=	cylinder length
l	=	plate length
n	=	total number of nodes inside V_{piezo}
p	=	pressure
R	=	resistance without mechanical stress
Re	=	Reynolds number
R_1, R_3	=	longitudinal piezoresistors
R_2, R_4	=	transversal piezoresistor
r	=	radius of a circular diaphragm
S	=	sensitivity of a pressure sensor
St	=	Strouhal number
Tu	=	turbulence level
t	=	thickness of a diaphragm
u_∞	=	upstream velocity
V_{off}	=	offset voltage
V_{out}	=	output signal of the Wheatstone bridge
V_{piezo}	=	volume of a piezoresistor
V_{supply}	=	supply voltage
x, y, z	=	Cartesian coordinates
Δp	=	differential pressure
ΔR	=	change of resistance at Δp
$\Delta R_{1,3}$	=	resistance change of the longitudinal piezoresistors
$\Delta R_{2,4}$	=	resistance change of the transversal piezoresistors
π_{44}	=	piezoresistance coefficient of p-type piezoresistors
$\sigma_{\text{ci;max}}$	=	maximum mechanical stress of a circular diaphragm
$\sigma_{\text{sq;max}}$	=	maximum mechanical stress of a square diaphragm
$\bar{\sigma}_x$	=	spatially averaged stress component in the x direction
$\sigma_{x;i}$	=	x component of mechanical stress at node i; parallel to diaphragm edge
$\bar{\sigma}_y$	=	spatially averaged stress component in the y direction
$\sigma_{y;i}$	=	y component of mechanical stress at node i, perpendicular to diaphragm edge
σ_{1x}	=	longitudinal stress component in the x direction at R_1
σ_{1y}	=	transversal stress component in the y direction at R_1
σ_{2x}	=	longitudinal stress component in the x direction at R_2
σ_{2y}	=	transversal stress component in the y direction at R_2

Presented as Paper 271 at the 46th AIAA Aerospace Sciences Meeting and Exhibit, Reno Nevada, 7–10 January 2008; received 6 March 2008; revision received 16 June 2008; accepted for publication 28 August 2008.

*Ph.D. Student, Microsensor & Actuator Technology Center, Gustav-Meyer-Allee 25; berns@mat.ee.tu-berlin.de. Student Member AIAA.
†Ph.D. Student, Microsensor & Actuator Technology Center, Gustav-Meyer-Allee 25. Member AIAA.
‡Professor, Microsensor & Actuator Technology Center, Gustav-Meyer-Allee 25.
§Research Engineer, Department of Fluid Mechanics, Albert-Einstein-Straße 2.
¶Professor, Department of Fluid Mechanics, Albert-Einstein-Straße 2.
**Ph.D. Student, Berlin, Institute of Fluid Mechanics and Engineering Acoustics, Müller-Breslau-Straße 8.
††Professor, Berlin, Institute of Fluid Mechanics and Engineering Acoustics, Müller-Breslau-Straße 8.

I. Introduction

MICRO-ELECTROMECHANICAL system (MEMS) sensors have proven to be of tremendous importance to the field of measurement engineering. Because of their versatility, excellent performance, low power consumption, and low manufacturing cost, many conventional devices have been replaced by MEMS sensors during the last decades. The application of MEMS to experimental fluid mechanics and flow research, often referred to as aeroMEMS, has been one of the most exciting developments in recent years [1–7].

The detection of wall pressure distributions has primarily been performed using the well-established pinhole method [8,9]. This method makes use of discrete pressure sensors connected to the

measurement surface via pressure taps and tubes. Depending on the experimental setup, the distance between the sensor and measurement surface can vary considerably. In typical pin hole setups, the dynamic properties of the pressure sensors suffer from frequency damping and reflection caused by tubing. An example of frequency damping is described by Johansen et al. [10]. They presented a fast-response, multihole probe with embedded ±1 psi differential pressure sensors. Because of the tubes used to connect the sensors to the front tip of the probe, the sensors' frequency response was reduced by a factor of approximately 6.

To avoid any connection-based damping, the sensor itself should be mounted flush with the surface. Thus, the dynamic response of the sensors is unaffected by the experimental setup. Recently developed pressure sensor arrays optimized for high-frequency response employ flush-mounted sensor chips. Measurement results show a substantially wider frequency range of pressure fluctuation signals than detected before [11,12]. However, due to the relatively large pressure ranges (up to 100 kPa) of the sensors employed, a low pressure resolution is obtained.

A different approach to avoid tubes between the sensors and the surface is the application of capacitive surface pressure sensor arrays. Zagnoni et al. [13] published the development of a thin-film strip fabricated by advanced printed circuit board (PCB) technology consisting of several capacitive pressure sensors based on a multilayer polymer structure. Because this array is designed for relatively large surfaces, the sensor area is extensive, resulting in a low frequency resolution. Palasagaram et al. developed a flexible capacitive sensor array consisting of 15 sensors featuring different circular diaphragm sizes (diameters from 2 to 4.8 mm) [14]. The differential pressure range was approximately 170 kPa. Because of the capacitive sensing principle, the output signals of these sensor arrays are strongly nonlinear.

For the characterization of static pressure distributions on surfaces of various shapes and sizes, the use of pressure sensitive paint (PSP) has proven to be a versatile measurement tool [15]. In recent years, the dynamic resolution of PSP has been improved. McGraw et al. described the application of PSP to the surface of a square cylinder to measure surface pressure fluctuations [16]. Results showed frequencies up to 125 Hz and a pressure resolution of approximately 70 Pa. A photo diode and a laser were necessary for the pressure readout. Calibration was performed with a microscope. The main disadvantages of PSP are the strong temperature dependence, the extensive data acquisition, and the low dynamic resolution.

The examples described show that different measurement techniques for the characterization of wall pressure and wall pressure fluctuation exist. All those methods exhibit different assets and drawbacks. According to the specific measurement task, the optimal sensing principle has to be employed.

For surface pressure measurements in low-velocity flows, pressure sensors with a pressure range of only a few hundred pascal are required. Because of the complexity and limited predictability of flow phenomena and their strong dependence on local geometry and aerodynamic conditions, it is most important to employ sensors providing high resolution and excellent dynamic properties. The AeroMEMS pressure sensors employed to assemble the arrays presented herein comply with these requirements.

Sensor array development, aerodynamic measurements, and flow simulation are conducted within the scope of the Imaging Measuring Methods for Flow Analysis research project funded by the German Research Foundation. The main objectives of this program are the development of new flow measurement techniques and the improvement of the performance of both existing and new techniques. To test newly developed measurement tools such as the sensor arrays presented herein, the complex unsteady flow around a wall-mounted finite cylinder at a Reynolds number of 200,000 is investigated. Optical measurements (laser Doppler anemometry, or LDA; particle image velocimetry, PIV) of such a flow have been conducted at the University of Rostock [17]. Numerical simulations of a model similar to the experimental setup have been performed at the Institute of Fluid Mechanics and Engineering Acoustics at the Berlin Institute of Technology [18].

II. Micro-Electromechanical System Pressure Sensor Design and Optimization

A. Basic Sensor Design

Highly sensitive MEMS pressure sensors either employ a capacitive or piezoresistive sensing principle [19]. The piezoresistive effect is the change of resistivity of a conducting material due to applied mechanical stress [20]. In comparison with capacitive sensors, piezoresistive sensors have the advantages of simple signal processing and excellent linearity.

Today's piezoresistive silicon pressure sensors typically consist of a square or circular diaphragm with four p-type piezoresistors connected to form a Wheatstone bridge [19]. The piezoresistors are arranged in parallel and perpendicularly to the edge of the diaphragm to make use of the longitudinal and transversal piezoresistive effect [20] (Fig. 1).

The pressure sensors presented feature a square diaphragm because of its higher sensitivity compared with a circular diaphragm with similar thickness t and a diameter D_{dia} equal to the side length a of the square diaphragm. The maximum mechanical stress at the edge of the diaphragm is a good indicator of the sensitivity of a pressure sensor. The maximum mechanical stresses of a square ($\sigma_{\text{sq;max}}$) and a circular ($\sigma_{\text{ci;max}}$) diaphragm subjected to the applied uniform differential pressure Δp are given by Eqs. (1) and (2) [21]:

$$\sigma_{\text{sq;max}} = \frac{0.3078 \cdot \Delta p \cdot a^2}{t^2} \tag{1}$$

$$\sigma_{\text{ci;max}} = 0.75 \cdot \frac{\Delta p \cdot r^2}{t^2} \tag{2}$$

where t is the diaphragm thickness, a is the width and length of a square diaphragm, and r is the radius of a circular diaphragm.

For the same diaphragm thickness t, differential pressure Δp, and $r = a/2$, the following relation is obtained:

$$\sigma_{\text{sq;max}}/\sigma_{\text{ci;max}} \approx 1.64 \tag{3}$$

The maximum stress at the edge of a square diaphragm is considerably higher than at the edge of a circular diaphragm. The use of a square diaphragm, therefore, can yield a more than 60% higher pressure sensitivity.

Figure 1 shows a square diaphragm with four p-type piezoresistors (boron doping) arranged to make use of the longitudinal (R_1, R_3) and transversal (R_2, R_4) piezoresistive effect. The resistors are oriented in ⟨110⟩ direction on an n-type (phosphorous doping) silicon wafer with (100) crystal orientation. It is assumed that the center of each resistor has the same distance from

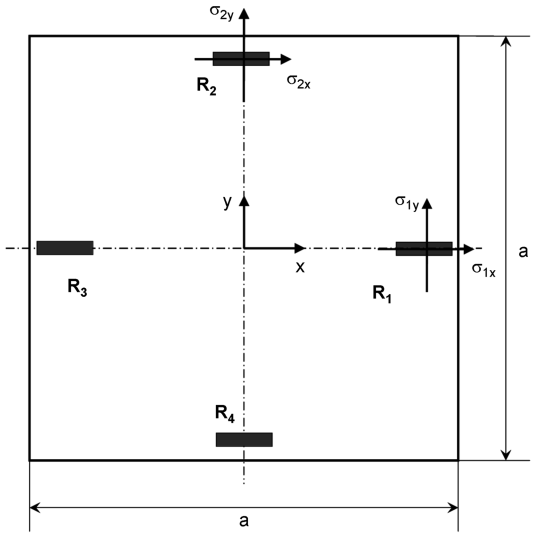

Fig. 1 Sensor diaphragm with four piezoresistors making use of the piezoresistive effect.

the diaphragm edge along the symmetry axis. Furthermore, the zero stress resistances of the longitudinal piezoresistors $R_{1,3}$ and the transversal piezoresistors $R_{2,4}$ are assumed to be equal. For a square diaphragm, the longitudinal stress component in the x direction, σ_{2x}, at R_2 is equal to the transversal stress component in the y direction, σ_{1y}, at R_1. Also, the transversal stress component in the y direction, σ_{2y}, at R_2 is equal to the longitudinal stress component in the x direction, σ_{1x}, at R_1 (see Fig. 1).

The change of the resistance, which depends on the mechanical stress that the longitudinal resistors R_1 and R_3 and the transversal resistors R_2 and R_4 are subjected to, can be calculated as follows:

$$\frac{\Delta R_1}{R_1} = \frac{\Delta R_3}{R_3} \approx \frac{\pi_{44}}{2}(\sigma_{1x} - \sigma_{1y}) = \frac{\Delta R}{R} \tag{4}$$

and

$$\frac{\Delta R_2}{R_2} = \frac{\Delta R_4}{R_4} \approx -\frac{\pi_{44}}{2}(\sigma_{2y} - \sigma_{2x}) = -\frac{\Delta R}{R} \tag{5}$$

where $\Delta R_{1,3}$ is the resistance change of the longitudinal piezoresistors, $\Delta R_{2,4}$ is the resistance change of the transversal piezoresistors, and π_{44} is the piezoresistance coefficient of the p-type piezoresistors. It is assumed that the resistance values of R_1, R_2, R_3, and R_4 are equal for evanescent mechanical stress.

The output signal $V_{\text{out}}(\Delta p)$ of the Wheatstone bridge can be determined by Eq. (6) [19]:

$$V_{\text{out}}(\Delta p) = V_{\text{off}} + \mathrm{V}_{\text{supply}}(\Delta R(\Delta p)/R) \tag{6}$$

where V_{off} is the offset voltage, V_{supply} is the supply voltage, $\Delta R(\Delta p)$ is the change of resistance at Δp, and R is the resistance without mechanical stress.

In the case of a balanced bridge, the offset voltage is zero. Thus, the change in resistance is directly converted into a change of output voltage: $\Delta V_{\text{out}}(\Delta p)$. The sensitivity S of the pressure sensor is then given by

$$S = (\Delta V_{\text{out}}/\Delta p) \cdot (1/\mathrm{V}_{\text{supply}}) \tag{7}$$

B. Design Optimization

To determine the sensitivity and nonlinearity of different diaphragm sizes and thicknesses, a finite element analysis was performed employing ANSYS. The symmetry of the square diaphragm allows for only one-eighth of the whole model to be simulated. For a diaphragm with uniform thickness and a given resistivity of the piezoresistors, two geometric parameters, diaphragm size and thickness, define the sensitivity of the pressure sensor. As shown in Sec. II.A, the parameter dominating the sensitivity is the mechanical stress on the surface of the diaphragm. To simulate mechanical stresses, a model of the sensor diaphragm featuring the size and thickness of the diaphragm as variables and the surface pressure as load is established. Changing the load while keeping the diaphragm thickness and size constant provides the results needed for the calculation of the sensitivity and nonlinearity. Pressure sensitivities for the various diaphragm sizes and thicknesses are calculated. Figure 2 shows the z deflection of one-eighth of a diaphragm (bulk material is also modeled) with an edge length of 900 μm and a thickness of 3 μm under a uniform pressure load of $\Delta p = 100$ Pa on the top side. A fixture of the chip at the bottom of the bulk material is used as the boundary condition. The maximum deflection of 0.24 μm occurs in the center of the diaphragm.

The mechanical stress component in the y direction (given in mega-Pascals) is depicted in Fig. 3. Its maximum (tensile stress) is located at the edge of the diaphragm. Its minimum (compressive stress) occurs at the corner that is formed by the etching process at the opposite side of the diaphragm (shown in Figs. 3 and 4).

Because of the high aspect ratio of diaphragm size to diaphragm thickness, submodelling had to be performed to gain maximum accuracy. A cutout of the original model (shown in Fig. 3) including the region of maximum mechanical stress is remodeled and discretized employing a substantially higher mesh density. Loads and deflections are transferred from the "coarse model" depicted in Fig. 3.

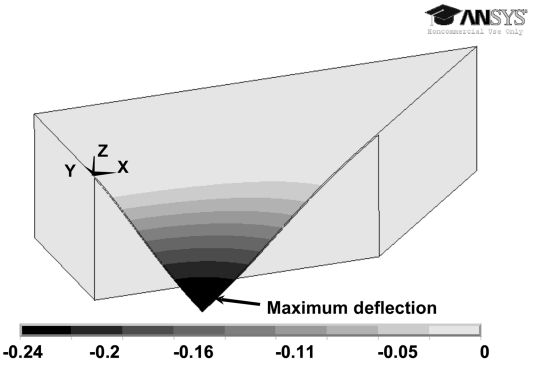

Fig. 2 Simulated mechanical z deflection (in micrometers) of a diaphragm due to applied pressure.

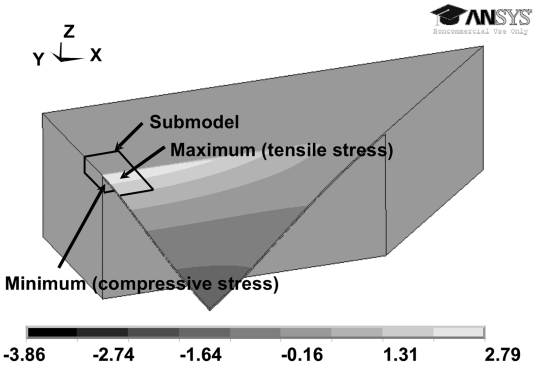

Fig. 3 Simulated mechanical stress in the y direction (in mega-Pascals) on an eighth of the sensor diaphragm.

Figure 4 shows a close-up view of the submodel and provides more detailed information about the mechanical stress component in the y direction (corresponding to the ⟨110⟩ direction in the silicon crystal) at the symmetry axis of the diaphragm (region of maximum stress). Mechanical stress is given in mega-Pascals, and its maximum is near the diaphragm edge. According to Eqs. (4–7), piezoresistors have to be placed in this region of maximum mechanical stress to ensure maximum sensitivity. For the used Wheatstone bridge configuration, the output signal for each fixed set of geometric parameters is calculated by Eqs. (5) and (6). In the previous paragraph, calculations of the mechanical stress were based on the geometric center of the resistors. Accurate values for the spatially averaged stress components are calculated by adding up the stress component (the x and y component) values at all nodes of the finite

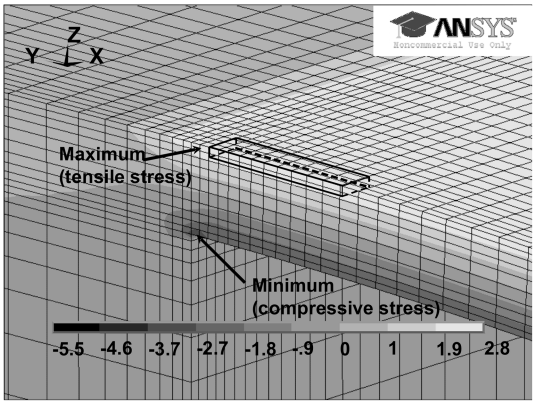

Fig. 4 Close-up view of the submodel showing the region of maximum mechanical stress.

element method model included in the volume of the piezoresistor V_{piezo}:

$$(\bar{\sigma}_y - \bar{\sigma}_x) = \frac{1}{n} \cdot \sum_{i=1}^{n} [\sigma_{y;i}(\Delta p, x, y, z) - \sigma_{x;i}(\Delta p, x, y, z)] \quad (8)$$

The spatially averaged stress has to be calculated for both the longitudinal and transversal piezoresistors. The appropriate placement of the piezoresistors ensures the equality of those averaged stresses. The output voltage of the sensor for a given differential pressure Δp is then calculated by Eq. (9):

$$V_{\text{out}}(\Delta p) = \mathrm{V}_{\text{supply}}(\pi_{44}/2) \cdot (\bar{\sigma}_y - \bar{\sigma}_x) \quad (9)$$

The doping concentration and p–n-junction depth of a piezoresistor depends on the implantation and annealing parameters (boron ion dose, implantation energy, annealing temperature, and time). These were calculated and optimized using SUPREM-IV [22]. The piezoresistance coefficient π_{44} for all calculations is taken from Tufte and Stelzer [23] using the spatially averaged doping concentration in the volume of the piezoresistor ($\pi_{44} \approx 95 \times 10^{-7}$ cm/N; p–n-junction depth $= 0.3$ μm).

Varying the applied pressure, the dependence of output voltage on pressure is calculated by Eq. (9). The sensitivities of the different sensor designs are subsequently calculated using Eq. (7).

Based on this approach, the sensitivity and linearity for various diaphragm sizes and thicknesses are predicted. Figure 5 shows the simulated sensitivities depending on diaphragm size (500–1100 μm) and thickness (2–6 μm). A diaphragm with a thickness of 3 μm and a size of 900×900 μm^2 exhibits a sensitivity of 11 μV/(VPa). The combinations of diaphragm thickness and size highlighted in Fig. 5 (thickness: 3 μm; sizes: 500, 700, and 900 μm) are chosen for fabrication. A linearity error of less than 1% (for all three sets of parameters) is predicted in a pressure range of ± 500 Pa.

Employing the same ANSYS model used for stress simulation, resonance frequencies for various diaphragm sizes and three different thicknesses are obtained by a modal analysis. For the three selected sets of diaphragm thickness and size, simulated resonance frequencies of 160 (500), 82 (700), and 50 kHz (900 μm) are determined.

C. Sensor Chip Layout

The final sensor chip layout is shown in Fig. 6. The positions of the piezoresistors and metallization are selected to provide the maximum sensitivity for the three different diaphragm sizes (the depicted layout has a diaphragm size of 500 μm). Aluminum metallization and bond pads enable gold wire bonding. A p–n diode for temperature measurement on the sensor surface is integrated into the silicon. The chip size is 2.5×4.5 mm^2. The relatively large overall chip size ensures safe and reliable handling during array assembly. Furthermore, flow disturbances due to bond wires near the sensing diaphragm are reduced.

The area confined within the square in Fig. 6 shows the piezoresistor layout with heavily doped contact areas and metallization and is enlarged in Fig. 7. Longitudinal piezoresistors are folded to keep them within the region of maximum mechanical stress near the diaphragm edge. The transversal piezoresistors are also divided to realize an equal resistivity of all four resistors.

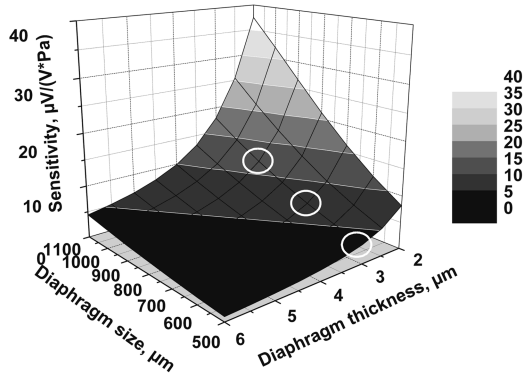

Fig. 5 Sensor sensitivity for various diaphragm sizes and thicknesses.

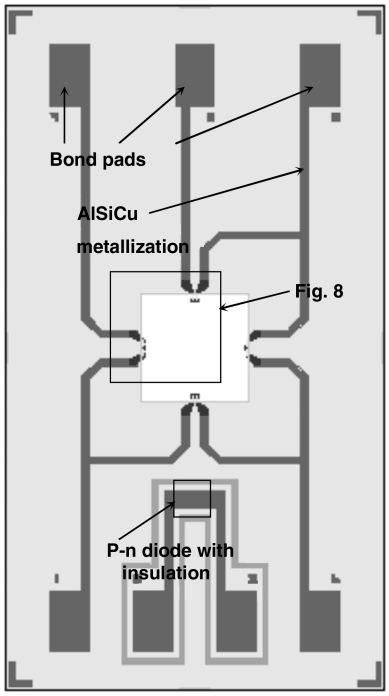

Fig. 6 Sensor chip layout.

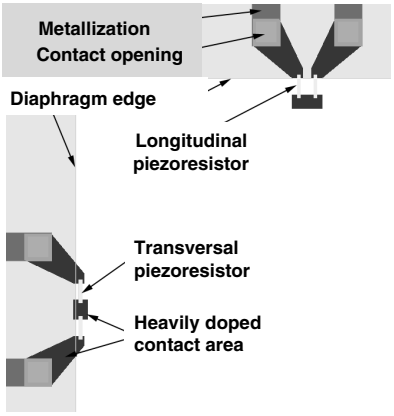

Fig. 7 Piezoresistor layout on the silicon diaphragm.

III. Sensor Fabrication and Characterization

A. Fabrication Process

The pressure sensors are fabricated by silicon micromachining [24]. Silicon-on-insulator wafers (n-type (100)-device layer) are used to obtain a uniform diaphragm thickness of 3 μm. The thicknesses of bulk silicon and buried oxide (BOX) are 300 and 0.4 μm, respectively.

The fabrication process flow is illustrated in Figs. 8a–8e. Initially, a 100 nm SiO_2 layer is grown by dry thermal oxidation at 1000°C (Fig. 8a). Two boron implantations are carried out to form the piezoresistors, implanted conductors, and the p-doped zone of the p–n diode (Fig. 8b). A phosphorous implantation completes the diode. Rapid thermal annealing provides shallow p–n junctions and activates the dopants [25].

To complete the passivation layer, silicon nitride (low-pressure chemical vapor deposition Si_3N_4) is deposited at 780°C (Fig. 8c). After opening the contact areas by dry and wet chemical etching

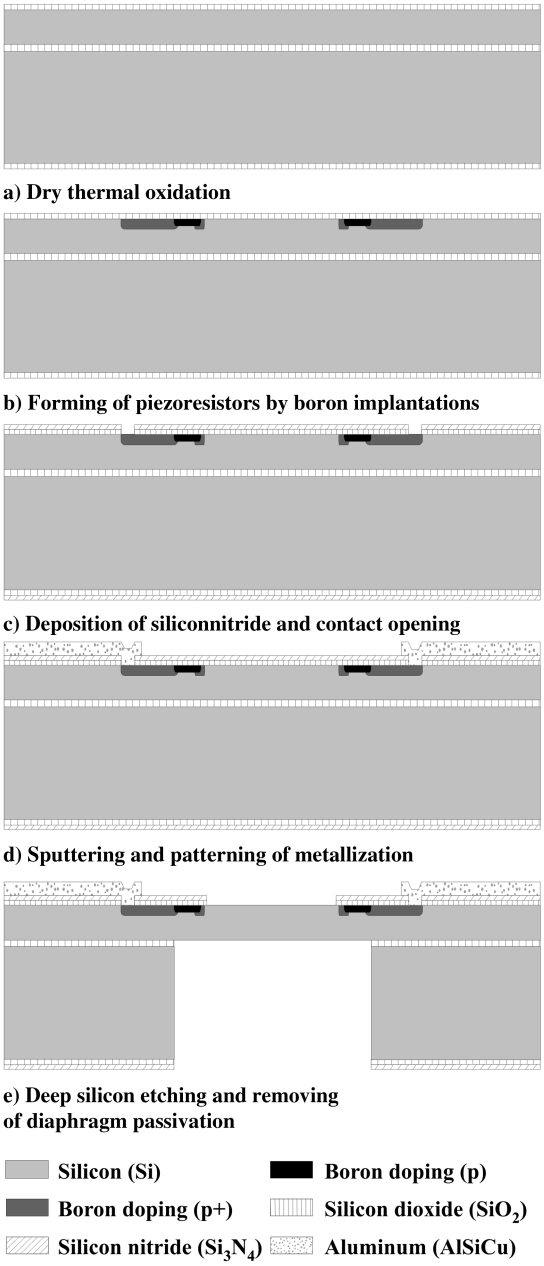

Fig. 8 Process flow for the manufacturing of piezoresistive MEMS pressure sensors.

(Fig. 8c), the AlSiCu metallization is sputtered and patterned, thus creating bond pads and conductors (Fig. 8d). An insulating trench surrounding the p–n diode is realized by the patterning of the passivation layers and the remaining silicon device layer (3 μm) using reactive ion etching.

The fabrication of the diaphragm is performed using an optimized Bosch process (Fig. 8e), featuring nearly vertical sidewalls (Fig. 9).

The BOX is used as an etch stop and is removed together with the remaining SiO_2 layer (Fig. 8e) on top of the diaphragm (the Si_3N_4 layer was removed previously) in buffered oxide etch.

Figure 10 shows a pressure sensor chip with a size of $2.5 \times 4.5 \times 0.3$ mm^3. The silicon diaphragm has a size of 900×900 μm^2 and appears translucent as the result of a thickness of only 3 μm.

In addition to the AlSiCu metallization including bond pads and conductors, the integrated p–n diode with the surrounding isolating trench is visible. Two different implantation areas, longitudinal and transversal piezoresistors with heavily doped zones, are framed and displayed in larger-scale scanning electron microscopy micrographs in Fig. 11.

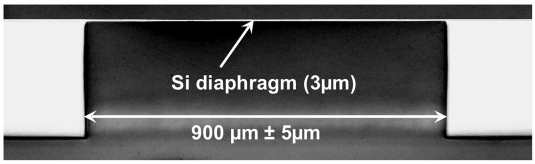

Fig. 9 Cross section of a silicon diaphragm realized by deep silicon etching employing a Bosch process.

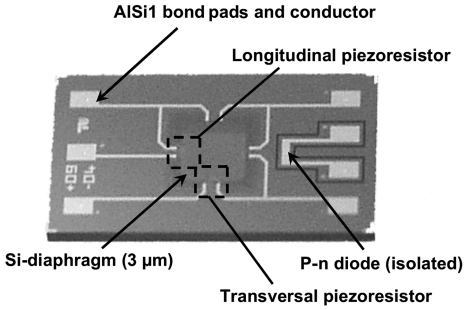

Fig. 10 Pressure sensor featuring a diaphragm size of 900 μm.

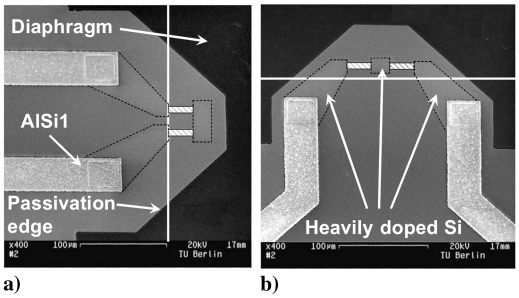

Fig. 11 SEM micrographs of the implanted piezoresistors: a) longitudinal, and b) transversa).

The piezoresistors are folded and electrically connected to the aluminum conducting paths via heavily doped implantation zones. The total length of one piezoresistor is 50 μm at a length-to-width ratio of 10. The longitudinal piezoresistors extend from the projected diaphragm edge (shown by the white line in Fig. 11) onto the diaphragm, whereas the transversal piezoresistors are located 10 μm away from the edge. To minimize diaphragm deformation due to internal stress caused by the different material layers, most of the diaphragm area is cleared of the passivation. Only the implanted areas on the diaphragm remain covered by a trapezoidal-shaped passivation. For the same reason, the AlSiCu conductors are placed on the bulk material at a distance of approximately 50 μm from the diaphragm edge.

B. Static Sensor Calibration

The fabricated sensors are characterized using a MENSOR calibration system (PCS-400) featuring an accuracy of 0.25 Pa. Measurements are carried out in a temperature chamber at temperatures between 15 and 40°C. Sensors are run with a supply voltage of 1 V.

To achieve high accuracy regarding the temperature and pressure, a custom-made calibration box was used. Figure 12 shows two calibration boxes inside a temperature chamber. Up to nine single sensors are glued to a PCB with photo resist and contacted by gold wire bonding. A closed-loop system is realized using O-ring seals on the top and bottom sides of the board. This allows for pressurization with a calibration pressure and a reference pressure. In addition, the sensors are protected from abrupt changes in environmental parameters caused by ventilation, temperature drift, and noise. A

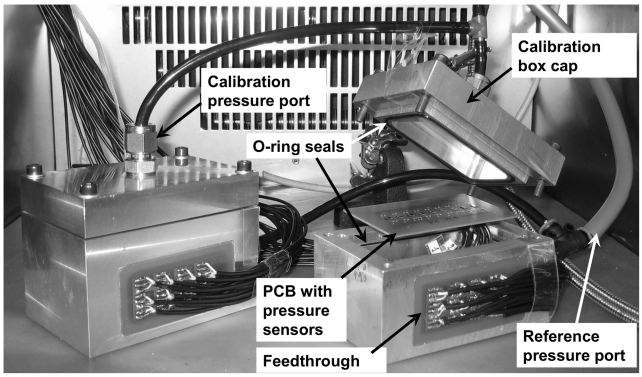

Fig. 12 Photo of the calibration boxes used for pressure and temperature calibration.

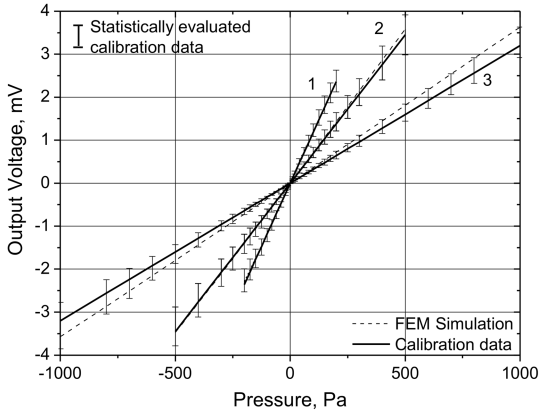

Fig. 13 Output voltages of the three different sensor types developed.

platinum resistor is used to measure the temperature inside the calibration chamber and provide signals for temperature control. For a readout of sensor signals and the provision of the supply voltage, the sensors are connected with the measurement equipment with a sealed feedthrough. Calibration using six temperature values takes approximately 8 h. To gain statistically evaluable calibration data, approximately 50 sensors of each type are characterized. The calibration results are compared with the simulated output signals described in Sec. II.B. Figure 13 shows the output voltages of the three different sensors developed vs the applied differential pressure. The scattering of measurement data is caused by the diaphragm thickness variations of the different sensor chips characterized. The error bars indicate the range of the measured sensitivities of the different sensors. The thickness variation of the device layer as specified by the wafer manufacturer is ± 0.5 μm.

The output signal drift of the pressure sensors is investigated using the same calibration box and measurement setup. Sensor signals are monitored (one measurement every 5 min) over a period of 24 h at a constant temperature of 25°C and a differential pressure of 0. Because of the temperature control loop and the high thermal capacity of the calibration box, the temperature deviation inside the boxes is lower than 0.1 K. The output signal drift should not exceed ± 10 μV in 24 h. Table 1 lists the sensor calibration data of the three different sensor types. The nonlinearity is determined by the maximum deviation between the calibration curve and the line of best fit (principle of minimum error). The pressure resolution is derived from the maximum hysteresis and sensitivity.

C. Dynamic Sensor Characterization

Measurements of the dynamic behavior are performed by subjecting sensor chips glued to a TO8 socket to a mechanical impulse. The output signal is amplified and analyzed with an oscilloscope. The resonance frequency is derived by Fourier transformation.

The measurement results are listed in Table 2 and compared with the simulated resonance frequencies. Measurements with sensors featuring a 500 μm diaphragm show no clear results because of the poor quality of the sensor output signal.

IV. Experimental Setup and Measurements

A. Experimental Setup

A truncated circular cylinder model is mounted on a ground plate (Fig. 14) and positioned in a Göttingen-type wind tunnel. The wind-tunnel flow is characterized by a low turbulence level of $Tu = 0.4\%$ in freestream and a blockage ratio of less than 8%. The circular cylinder has a diameter of $D = 120$ mm and an aspect ratio of $L/D = 2.0$. Measurements are performed at a Reynolds number (Re) of 200,000 based on the diameter D. This Reynolds number is obtained by an upstream velocity u_{oo} of 26 m/s. The ground plate has a length of 1300 mm and a thickness of 15 mm. The trip wire is necessary to establish a defined inflow boundary condition at the beginning of the plate. This setup was chosen to investigate the developing unsteady flowfield and corresponding wall pressure distributions at the cylinder model and ground plate.

The flowfield around the cylinder was examined preliminary by a three-component LDA. The results are briefly described in Sec. IV.B.

B. Flow Topology Around the Wall-Mounted Finite Cylinder

The experimental setup presented in Sec. IV.A will induce a turbulent flowfield with recirculation areas. Laser Doppler anemometry is

Table 1 Calibration data for the three different fabricated pressure sensor types

Diaphragm size, μm	500	700	900
Pressure range, kPa	± 1.0	± 0.6	± 0.2
Nonlinearity		$<1\%$	
Sensitivity, μV/(VPa)	3	7	12
Pressure resolution, Pa	2	1	0.5
Offset voltage, mV		$< \pm 3$	
Temperature coefficient of the offset, %/K		-0.07	
Temperature coefficient of the sensitivity, %/K		-0.18	
Output voltage drift, μV		$< \pm 10/24$ h	
Temperature coefficient of the p–n diode, mV/K		-1.8 (with supply current of 100 μA)	

Table 2 Comparison of simulated and measured resonance frequencies for the different sensor types

Diaphragm size	900 μm	700 μm	500 μm	Unit
Resonance frequency (simulation)	50	82	160	kHz
Resonance frequency (measurement)	45	65	>100	kHz

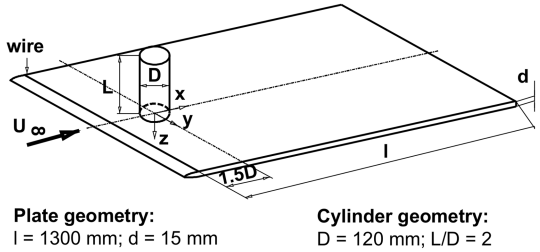

Fig. 14 Experimental setup with the truncated cylinder mounted on a ground plate.

an excellent method for nonintrusive flow exploration. Experimental results of three-component LDA investigations on a similar setup are published by Leder [17]. Figure 15 shows the time averaged velocity field around the cylinder measured by LDA. Flow patterns in the symmetry plane behind the cylinder (perpendicular to the ground plate) and in a plane parallel to the ground plate close to the foot region of the cylinder are visualized. Points Cy and Cz mark the centers of large separation zone vortices; point R is the reattachment point at the end of the recirculation region. B indicates the separation bubble on the free end of the cylinder.

These results are suited for a brief description of the flow topology around the wall-mounted finite cylinder.

The basic topological model shown in Fig. 16 visualizes the main features of the three-dimensional separated flow behind the cylinder model. It features the following different characteristic structures: 1) the region of laminar flow in front of the cylinder; 2) the three-dimensional flow structure with a small separation bubble on the free end of the cylinder; 3) a pair of side tip vortices separating from the top of the cylinder; 4) Kármán-type vortex shedding with typical oscillating behavior in the middle section of the cylinder; 5) the flow over the free end and downward in lee of the cylinder, splitting into a reattaching and a recirculating part; 6) the large region of separated flow formed by a U-shaped vortex core; and 7) the horseshoe vortex system in the foot region of the cylinder.

In some of the regions, the flowfield has a significant impact on the wall pressure distribution. The expected wall pressure distribution is described briefly.

The laminar boundary layer flow in the middle and upper sections at the front side of the cylinder results in a positive differential pressure distribution with low fluctuation intensity. The high pressure level at the stagnation line drops along the cylinder surface and reaches its minimum at an angle of about 70 deg (related to inflow at 0 deg). The increasing pressure gradient initiates the separation of the boundary-layer flow near 80 deg and merges into the free lateral shear layers. For the given Reynolds number, the point of flow transition from laminar to turbulent is expected in the free

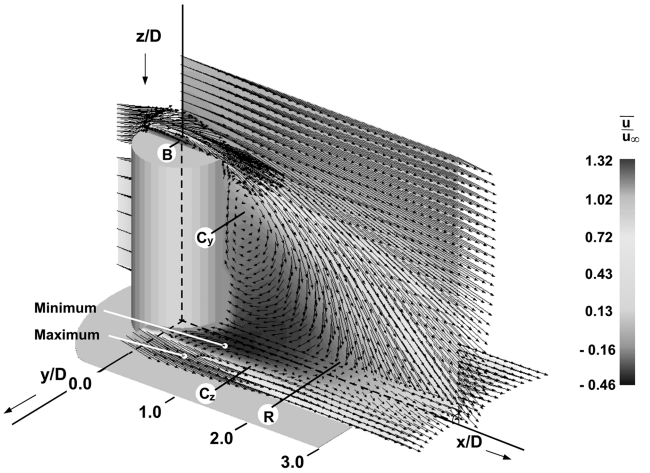

Fig. 15 Time averaged velocity field in two planes perpendicular to each other [17].

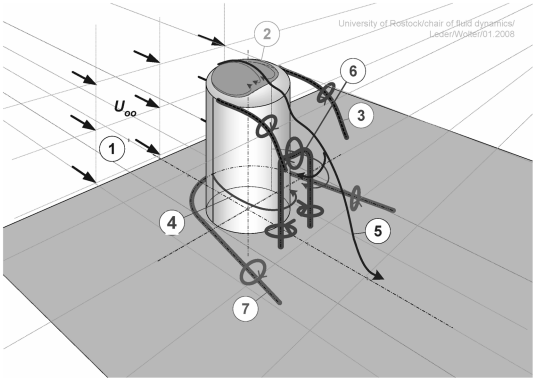

Fig. 16 Topological model of the flowfield around the wall-mounted cylinder.

shear layer closely behind the separation line. The separated turbulent shear layers along the side wall of the cylinder finally induce a vortex shedding process similar to a Kármán vortex shedding. Therefore, enhanced wall pressure fluctuations can be expected near the lateral separation lines.

The flow inside the separation bubble on the top of the cylinder model is shown in Figs. 17 and 18. The flow separates at the leading edge of the cylinder and reattaches downstream, which should produce an inhomogeneous negative differential pressure distribution on the top of the cylinder. The flow inside the separation bubble and along the side wall of the cylinder model induces two side tip vortices.

In summary, unsteady behavior of the wall pressure is expected as a result of different cyclic and stochastic flow phenomena. A high intensity of wall pressure fluctuations is expected along separation lines, in reattachment zones, and in the vicinity of vortex axes.

It should be noted that no dominant frequency of the vortex shedding, as in the case of an infinite cylinder, could be observed for the truncated cylinder. Here the fluctuations are more stochastic. The characteristic frequency of 43 Hz for an infinite long cylinder, related to a Strouhal number of $St = 0.2$, has been blurred into a broad range frequency spectrum with a peak value at $St = 0.16$ (35 Hz). The large three-dimensional separated flow region downstream shows a U-shaped axis.

C. Numerical Simulation

The cylinder configuration described earlier has been investigated numerically to obtain a well-established understanding of the flow

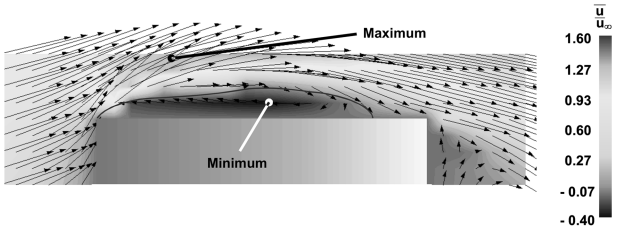

Fig. 17 Velocity field inside and around the separation bubble in the plane of symmetry ($y = 0.0$) [17].

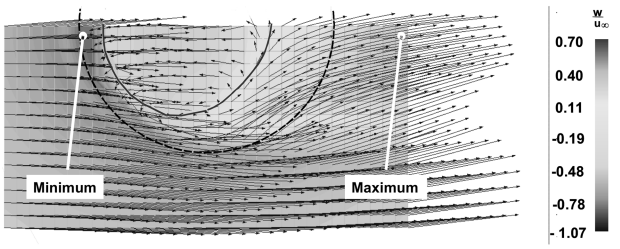

Fig. 18 Velocity field inside and around the separation bubble in the plane $z/D = -2.05$ [17].

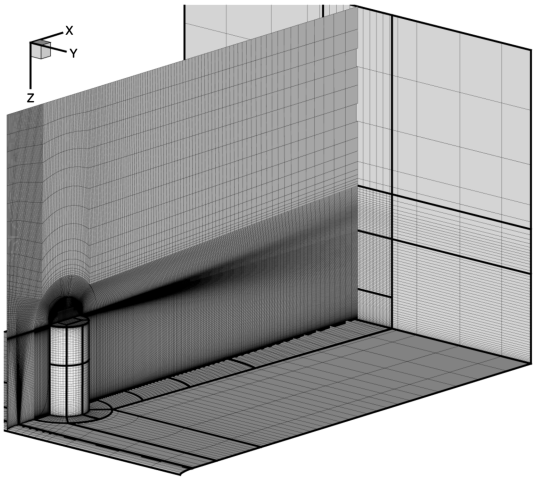

Fig. 19 Block-structured discretization of the wall-mounted cylinder model with 12.5 million grid points.

around it. To this end, the ambient fluid region has been discretized such that the spatiotemporal resolution satisfies the requirements for a well-resolved large-eddy simulation (LES) at the present Reynolds number. The computational grid consists of nearly 12.5 million cells with 10 million of the cells concentrated close to the cylinder and its wake. Figure 19 shows the grid for numerical simulation; on the walls and at the outflow only every third grid line is depicted. No-slip conditions are applied to all physical walls; the upper and the lateral boundaries feature a slip condition. A convective outflow boundary condition is applied to the downstream boundary. A spatially variable inlet velocity profile accounts for the blockage of the cylinder.

The solver used has been developed at the Institute of Fluid Mechanics and Engineering Acoustics [26]. It can be used to solve the Reynolds-averaged, filtered, or full Navier–Stokes equations according to the RANS, LES, or direct numerical simulation approach, respectively. Different subgrid scale (SGS) models with varying complexity are implemented in this code, which uses a conservative finite volume discretization based on general curvilinear coordinates. It is of second-order accuracy in time and space. As a result of the high grid resolution, the standard Smagorinsky SGS model [27] is sufficient to model the energy dissipation in the unresolved scales. The model constant has been set to 0.1.

To provide a statistical description of the flow similar to most experimental results, the predicted turbulent flowfield has been time averaged over 230 convective units D/u_∞. The resulting flow topology is shown in Fig. 20 [28]. The simulated flow topology shows very good agreement with the flow topology obtained from the LDA measurements.

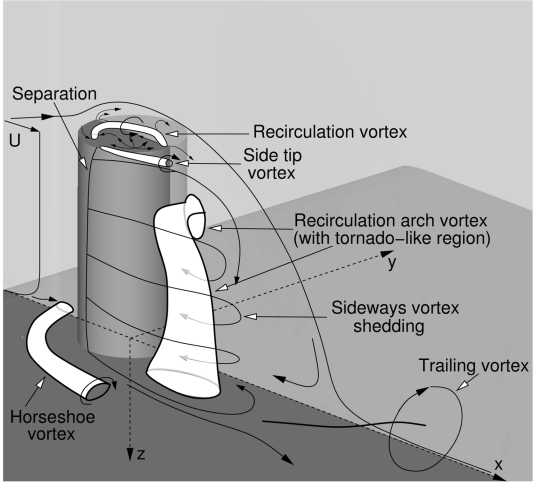

Fig. 20 Time averaged flow topology (not to scale) [28].

In front of the cylinder, the boundary layer on the plate stagnates, thus constituting a horseshoe vortex. On the top of the cylinder, a complex recirculation region is surrounded by the oblique separation at the leading edge and the reattachment close to the trailing edge. Behind the separation region on the cylinder shell close to 80 deg, typical alternate vortex shedding is generated but is disturbed massively by the flow over the free end. A recirculation arch vortex is formed by the combination of these phenomena; thus, the main flow reattaches to the plate. Trailing vortices are generated near this reattachment region by superimposed velocity components. The analysis reveals that, for this small cylinder aspect ratio, no coherent longitudinal vortices exist in the whole wake, as stated by most investigations on finite cylinders [28].

D. Integration of MEMS Pressure Sensor Arrays into the Surface of the Cylinder

Figure 21 shows the instrumentation for the time resolved determination of wall pressure distributions on the cylinder surface. The cylinder is equipped with MEMS surface sensor arrays and rotated around its vertical axis to obtain measurement data on the whole surface. A multichannel measurement system (SCXI/PXI components by National Instruments) is used for signal conditioning and data acquisition. Pressure sensors can be calibrated employing a Mensor pressure controller system (PCS-400).

Figures 22a–22d depict the cylinder equipped with a total of 48 MEMS pressure sensors. Three different types of surface sensor arrays were developed and mounted flush with the surface of the cylinder to avoid flow disturbances. A PCB) featuring 13 integrated sensors is located on the top of the cylinder (Fig. 22a). Four vertical sensor arrays (Fig. 22c and 22d) and a horizontal sensor array (Fig. 22b) are mounted flush with the curved surface of the cylinder.

Employing a special alignment technique, sensors are embedded into the arrays with a silicon adhesive [25]. Electrical contacts are realized by gold wire bonding. The back sides of the sensor arrays are sealed and connected to the pressure calibration system. Output signals are transferred via wire connections to a multichannel measurement system for processing.

E. Measurement and Data Processing

Figure 23 is a diagram of the instrumentation depicted in Fig. 21. To gain wall pressure data on the whole surface of the cylinder, measurements are repeated after a stepwise rotation by 5 deg of the cylinder.

During the experiment, the temperature in the wind tunnel is recorded. Calibrations are carried out during the experiment and allow the temperature drift of the sensors to be determined. Using the calibration matrix obtained during data postprocessing, the output signals are converted into pressure values and corrected for the temperature drift. Each measurement step is 30 s long. A sample frequency of 2 kHz and a low-pass filter frequency of 1 kHz are used. Test measurements with an increased sample frequency showed no characteristic flow phenomena above 1 kHz.

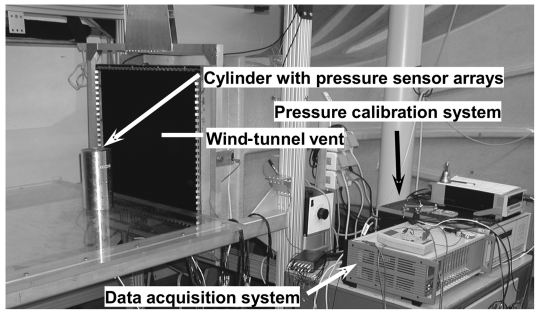

Fig. 21 Wall-mounted cylinder and the experimental setup with instrumentation.

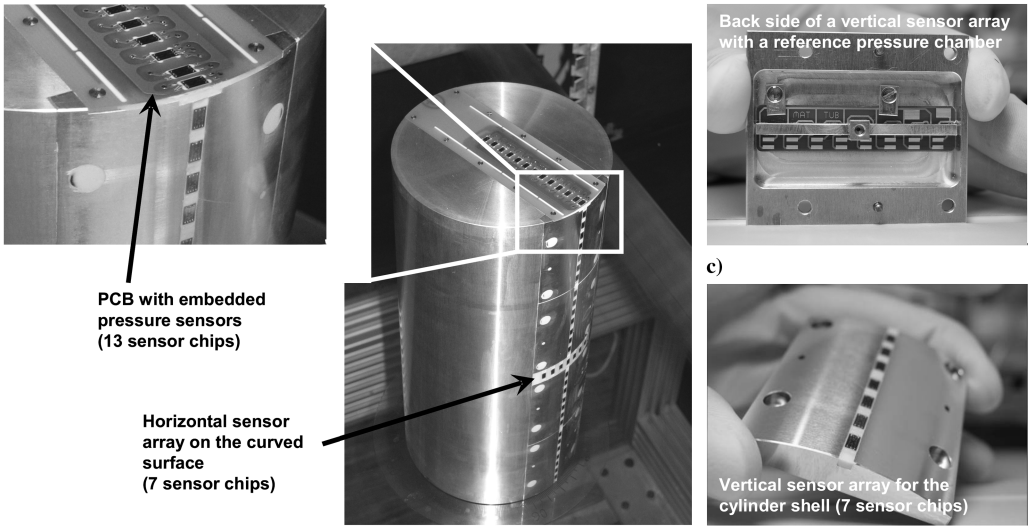

Fig. 22 Wall-mounted finite cylinder equipped with 48 MEMS pressure sensors.

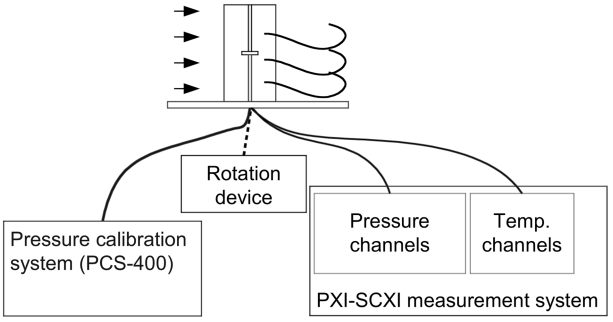

Fig. 23 Measurement instrumentation.

V. Results

A. Time Averaged Surface Pressure Distribution

The contour plots in Figs. 24a and 24b visualize the time averaged pressure distribution on the surface of the cylinder (Fig. 24a) and the corresponding results of a large-eddy simulation (Fig. 24b) [18]. The grayscale bar indicates the level of the surface pressures for both plots. The region of high differential impact pressure extends from 0 to 30 deg (0 deg refers to the position on the cylinder where the flow is perpendicular to the cylinder surface). In the region of the laminar boundary layer between 30 and 70 deg, the differential pressure decreases to a negative value. The pressure gradient increases until separation occurs (between 80 and 85 deg). Above 85 deg, the pressure is nearly constant.

Based on the LDA measurements, these measurement results have been predicted in Sec. IV.B. Although the simulated pressure distribution shows a lower negative differential pressure in the region of transition, the results are very comparable.

Figure 25 gives detailed information about the pressure distribution on the top of the cylinder. In contrast to the magnitude of pressure variation on the cylinder shell, the pressure range is only 100 Pa. Negative differential pressure values occur on the whole surface. The existence of regions of negative differential pressure has also been predicted in Sec. IV.B and is caused by the separation bubble on the top side of the cylinder.

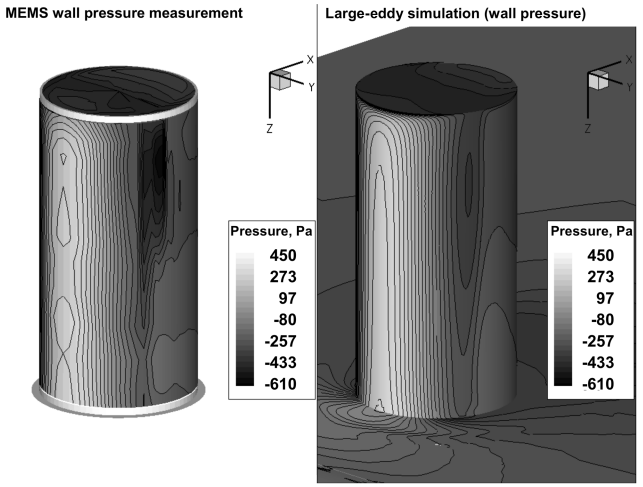

Fig. 24 Experimentally determined time averaged surface pressure distribution compared with the results of LES.

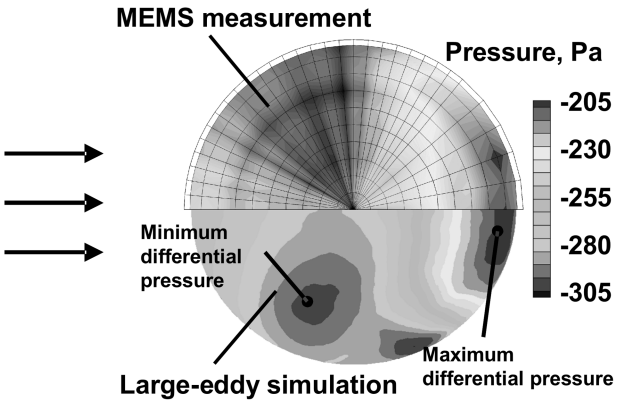

Fig. 25 Time averaged surface pressure on the top of the cylinder (measurement and simulation).

B. Time Resolved Surface Pressure

Figure 26 shows the experimentally determined fluctuation intensity (standard deviation of the time resolved wall pressure) on the surface of the cylinder. In the region of laminar flow between 0 and 30 deg, the fluctuation intensity has its minimum. The maximum fluctuation intensity occurs between 80 and 85 deg and correlates to the region of flow separation. On the top of the cylinder, the maximum fluctuation intensity is located at the positions where the side tip vortices separate from the cylinder (marked in Fig. 26). The

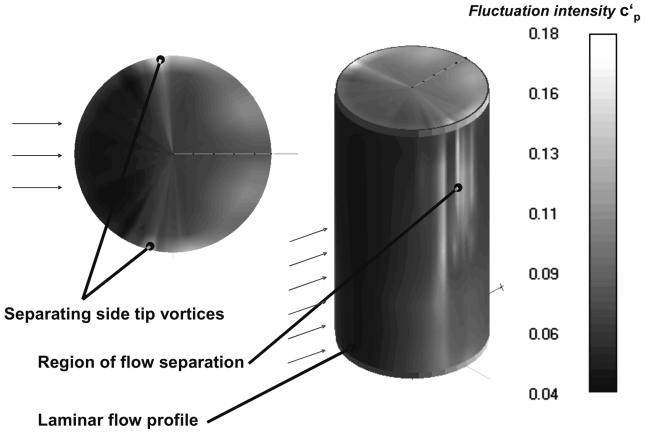

Fig. 26 Pressure fluctuation intensity on the surface of the cylinder.

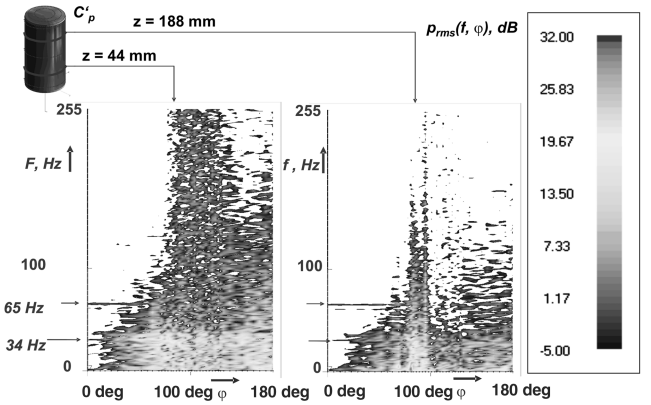

Fig. 27 Evaluation of the frequency distribution at two different heights on the cylinder shell.

flow features around the cylinder generating such a pressure distribution are discussed in Sec. IV.B.

To gain information about the spatial frequency distribution on the surface of the cylinder, time resolved measurement data are analyzed using fast Fourier transform. The frequency distributions along the circumference of the cylinder at two different distances from the ground plate ($z = 44$ and 188 mm) are plotted against the angle in Fig. 27. An angle of 0 deg marks the stagnation line (inflow direction). Both in the lower and upper parts of the cylinder, specific frequency peaks at 34 and 65 Hz are detected. In the laminar flow region, fluctuation frequencies remain below 50 Hz. The highest fluctuation frequencies occur at the separation line and are detected at both heights investigated. In the upper part of the cylinder, the highest fluctuation frequencies are limited to the region of separation whereas a broad range frequency distribution dominates at the lower part of the cylinder.

VI. Conclusions

Highly sensitive aeroMEMS pressure sensors were designed, fabricated, and characterized. To enable spatially distributed and time resolved measurements of flow-induced wall pressure on a wall-mounted finite circular cylinder, different surface sensor arrays were designed, realized, and installed. Wall pressure measurements at a Reynolds number of 200,000 were conducted at the University of Rostock in a wind tunnel. Experimental results show the excellent performance of the pressure sensors regarding sensitivity and dynamic properties and prove them to be a powerful measurement tool in experimental fluid mechanics. Experimentally determined results are very consistent with the results of a large-eddy simulation. Wall pressure fluctuation data are obtained, analyzed, and compared with the results of the LDA measurements. Combining established flow measurement techniques such as LDA and PIV with the presented wall pressure measurement technology, extensive information about the structure of turbulent flows around blunt structures can be obtained. The comparison of experimental results with numerical simulations allows the drawing of conclusions about the quality of flow simulations. To further optimize the sensor setup, the development of pressure sensors featuring sealed through-wafer vias facilitating back side contacts is in process [29].

Acknowledgments

Financial support by the Deutsche Forschungsgemeinschaft (DFG SPP 1147) is gratefully acknowledged. The numerical simulations were performed on the IBM pSeries 690 Supercomputer of the North German Cooperation of High-Performance Computing (HLRN).

References

[1] Löfdahl, L., and Gad-el-Hak, M., "MEMS Applications in Turbulence Flow Control," *Progress in Aerospace Sciences*, Vol. 35, No. 2, 1999, pp. 101–203. doi:10.1016/S0376-0421(98)00012-8

[2] Cho, S. T., Najafi, K., Lowman, C. E., and Wise, K. D., "An Ultrasensitive Silicon Pressure-Based Microflow Sensor," *IEEE Transactions on Electron Devices*, Vol. 39, No. 4, 1992, pp. 825–835. doi:10.1109/16.127472

[3] Arnold, D. P., Gururaj, S., Bhardwaj, S., Nishida, T., and Sheplak, M., "A Piezoresistive Microphone for Aeroacoustic Measurements," *Proceedings of the ASME International Mechanical Engineering Congress and Exposition*, American Society of Mechanical Engineers, New York, 2001, pp. 281–288.

[4] Liwei, L., and Weijie, Y., "MEMS Pressure Sensors for Aerospace Applications," *Proceedings of the IEEE Aerospace Conference*, Inst. of Electrical and Electronics Engineers, New York, 1998, pp. 429–436.

[5] Schiffer, M., Obermeier, E., Grewe, F., Ebner, A., and Fernholz, H. H., "AeroMEMS Surface Fence for Wall Shear Stress Measurements in Turbulent Flows," AIAA Paper 2006-0645, 2006.

[6] Buder, U., Berns, A., Petz, R., Nitsche, W., and Obermeier, E., "AeroMEMS Wall Hot-Wire Anemometer on Polyimide Substrate Featuring Top Side or Bottom Side Bondpads," *IEEE Sensors Journal*, Vol. 7, No. 8, 2007, pp. 1095–1101. doi:10.1109/JSEN.2007.897933

[7] Buder, U., Berns, A., von Klitzing, J.-P., Petz, R., Nitsche, W., and Obermeier, E., "Family of Micromachined Wall Hot-Wire Sensors on Polyimide Foil," *AIAA Journal*, Vol. 45, No. 8, 2007, pp. 1798–1809. doi:10.2514/1.25033

[8] Willmarth, W. W., and Wooldridge, C. E., "Measurements of the Fluctuating Pressure at the Wall Beneath a Thick Turbulent Boundary Layer," *Journal of Fluid Mechanics*, Vol. 14, 1962, pp. 187–210. doi:10.1017/S0022112062001160

[9] Boone, A. R., and Ulbrich, N., "The Development of a Wall Pressure Measurement System for Two NASA Ames Wind Tunnels," AIAA Paper 2002-3250, 2002.

[10] Johansen, E. S., Allen, R. D., and Rediniotis, O. K., "Embedded-Sensor Fast-Response Multi-Hole Probes," AIAA Paper 2003-1091, 2003.

[11] Tanielian, M. H., and Kim, N. P., "Pressure Belt: an integrated multisensor system," *Proceedings of the IEEE Sensors*, Inst. of Electrical and Electronics Engineers, New York, 2002, pp. 1182–1187.

[12] Leger, T. J., Johnston, D. A., and Wolff, J. M., "Flex Circuit Sensor Array for Surface Unsteady Pressure Measurements," *Journal of Propulsion and Power*, Vol. 20, No. 4, 2004, pp. 754–758. doi:10.2514/1.9842

[13] Zagnoni, M., Golfarelli, A., Callegari, S., Talamelli, A., Bonora, V., Sangiorgi, E., and Tartagni, M., "A Non-Invasive Capacitive Sensor Strip for Aerodynamic Pressure Measurement," *Sensors and Actuators A (Physical)*, Vol. 123–124, 2005, pp. 240–248. doi:10.1016/j.sna.2005.03.049

[14] Palasagaram, J. N., and Ramadoss, R., "MEMS Capacitive Pressure Sensor Array Fabricated Using Printed Circuit Processing Techniques," *IECON Thirty-First Annual Conference of the IEEE Industrial Electronics Society*, Inst. of Electrical and Electronics Engineers, New York, 2005, pp. 2357–2362.

[15] Bell, J. H., Schairer, E. T., Hand, L. A., and Mehta, R. D., "Surface Pressure Measurements Using Luminescent Coatings," *Annual Review of Fluid Mechanics*, Vol. 33, No. 1, 2001, pp. 155–206. doi:10.1146/annurev.fluid.33.1.155

[16] McGraw, C. M., Bell, J. H., Khalil, G., and Callis, J. B., "Dynamic Surface Pressure Measurements on a Square Cylinder with Pressure

Sensitive Paint," *Experiments in Fluids*, Vol. 40, No. 2, 2006, pp. 203–211.
doi:10.1007/s00348-005-0059-8

[17] Leder, A., "3D-Flow Structures Behind Truncated Circular Cylinders," American Society of Mechanical Engineers Paper FEDSM2003-45083, 2003.

[18] Frederich, O., Wassen, E., and Thiele, F., "Flow Simulation Around a Finite Cylinder on Massively Parallel Computer Architecture," *Proceedings of the International Conference on Parallel Computational Fluid Dynamics*, Elsevier, New York/Amsterdam, 2005, pp. 85–93.

[19] Sze, S. M., *Semiconductor Sensors*, Wiley, New York, 1994, Chap. 4.

[20] Smith, C. S., "Piezoresistance Effect in Germanium and Silicium," *Physical Review*, Vol. 94, 1954, pp. 42–49.
doi:10.1103/PhysRev.94.42

[21] Young, W. C., *ROARK'S Formulas for Stress and Strain*, 6th ed., McGraw–Hill, New York, 1986, pp. 440–464.

[22] Law, M. E., and Dutton, R. W., "Verification of Analytic Point Defect Models Using SUPREM-IV," *IEEE Transactions on Computer-Aided Design of Integrated Circuits and Systems (1982-) / IEEE Trans Comput-Aided Des*, Vol. 7, No. 2, 1988, pp. 181–190.
doi:10.1109/43.3148

[23] Tufte, O. N., and Stelzer, E. L., "Piezoresistive Properties of Silicon Diffused Layers," *Journal of Applied Physics*, Vol. 34, 1963, pp. 313–318.
doi:10.1063/1.1702605

[24] Berns, A., Buder, U., Obermeier, E., Wolter, A., and Leder, A., "AeroMEMS Sensor Array for High-Resolution Wall Pressure Measurements," *Sensors and Actuators A (Physical)*, Vol. 132, 2006, pp. 104–111.
doi:10.1016/j.sna.2006.04.056

[25] Hane, M., and Matsumoto, H., "A Model for Boron Short Time Annealing After Ion Implantation," *IEEE Transactions on Electron Devices*, Vol. 40, No. 7, 1993, pp. 1215–1221.
doi:10.1109/16.216424

[26] Xue, L., "Entwicklung eines effizienten parallelen Lösungsalgorithmus zur dreidimensionalen Simulation komplexer turbulenter Strömungen," Ph.D. Dissertation, Berlin Institute of Technology, Berlin, 1998.

[27] Smagorinsky, J., "General Circulation Experiments with the Primitive Equations," *Monthly Weather Review*, Vol. 91, 1963, pp. 99–164.
doi:10.1175/1520-0493(1963)091<0099:GCEWTP>2.3.CO;2

[28] Frederich, O., Wassen, E., Thiele, F., Jensch, M., Brede, M., Hüttmann, F.,and Leder, A., *Numerical Simulation of the Flow Around a Finite Cylinder with Ground Plate in Comparison to Experimental Measurements*, edited by C. Tropea, S. Jakirlic, H.-J., Heinemann, R. Henke, and H. Hönlinger, Vol. 96, Notes on Numerical Fluid Mechanics and Multidisciplinary Design, Springer, Berlin/Heidelberg/New York, 2007, pp. 348–355, ISBN 978-3-540-74458-0.

[29] Berns, A., Ngo, H.-D., Buder, U., and Obermeier, E., "AeroMEMS Pressure Sensor Array Featuring Through-Wafer Vias for High-Resolution Wall Pressure Measurements," *Proceedings of the 21st IEEE International Conference on Micro Electro Mechanical Systems*, Inst. of Electrical and Electronics Engineers, New York, 2008, pp. 896–899.

A. Naguib
Associate Editor